Tunnel Magnetoresistance in Self-Assemblies of Exchange-Coupled Core/Shell Nanoparticles

Fernando Fabris,[1] Enio Lima Jr.,[1] Cynthia Quinteros,[1] Lucas Neñer,[1] Mara Granada,[1] Martín Sirena,[1] Roberto D. Zysler,[1] Horacio E. Troiani,[1] Victor Leborán,[2] Francisco Rivadulla,[2] and Elin L. Winkler[1],*

[1]*Centro Atómico Bariloche, CNEA-CONICET, Avenida Bustillo 9500, Bariloche, Río Negro, Argentina*

[2]*Centro Singular de Investigación en Química Biolóxica e Materiais Moleculares (CIQUS), Departamento de Química-Física, Universidade de Santiago de Compostela, Santiago de Compostela 15782, Spain*

We report the precise control of tunneling magnetoresistance (TMR) in devices of self-assembled core-shell $Fe_3O_4/Co_{1-x}Zn_xFe_2O_4$ nanoparticles ($0 \leq x \leq 1$). Adjusting the magnetic anisotropy through the content of Co^{2+} in the shell, provides an accurate tool to control the switching field between the bistable states of the TMR. In this way, different combinations of soft-hard and hard-soft core/shell configurations can be envisaged for optimizing devices with the required magnetotransport response.

I. INTRODUCTION

The possibility to manipulate the electrical resistive state of magnetic/nonmagnetic multilayers by an external magnetic field (giant magnetoresistance, GMR) has already been demonstrated 30 years ago [1,2]. The strong coupling between the electron spin and charge degrees of freedom and the development of the tools for their manipulation, triggered the growth of a new field called spintronics [3,4]. The fabrication of magnetic tunnel junctions (MTJs) constitutes one of the most important advances in this field since then [5,6]. A MTJ is composed of two layers of ferromagnetic conductors separated by an insulating tunneling barrier, typically of approximately 1 nm. The different density of states at the Fermi level, $N(E_F)$, of the spin up and down subbands of the ferromagnetic metals imply a spin-dependent tunneling probability. Therefore, the electrical resistance of the device switches between high and low resistance states as the magnetic field changes the relative orientation of the magnetizations of the two magnetic layers (tunneling magnetoresistance, TMR). The MTJ devices present high versatility and a great degree of functionalization, allowing electrodes and barriers of different nature to be combined, where large tunneling magnetoresistance, up to hundreds of percents at room temperature, has been obtained [7,8]. However, their fabrication is a challenge, involving advanced thin-film deposition techniques and complex microfabrication procedures. Tunneling magnetoresistance has also been studied in simpler nanostruc-

tures as granular or disordered single films [9,10], where the grain boundaries act as tunnel barriers. However, the characteristic of the barrier cannot be controlled in these nanostructures and lower TMR values were obtained.

On the other hand, the spectacular advances of the chemical synthetic methods produced over the last few years, offer an affordable route for the synthesis of complex nanostructures, with a precise control of their chemical composition, shape, and size [11]. These can be assembled in crystal-like structures over large areas, in which the organic capping layer or a nonmagnetic shell protecting the particles acts as a tunneling barrier that controls the electronic transport. [12–17] Spin-dependent electrical transport and large magnetoresistance is also observed in devices formed by assembling conducting magnetic nanoparticles (MNPs) [14,18,19] or binary nanoparticle superlattices [20–22].

However, an important challenge that must be addressed in this field is the design of strategies to tune the switching field of the TMR devices, which is entirely determined by the anisotropy of the magnetic material [9,10,23–26]. Therefore, a good handling over the coercivity of the magnetic nanoparticles would allow the control over the TMR of the assemblies, in a similar approach as that used in multilayers [27].

In this regard, an exciting possibility is the fabrication of devices based on self-assemblies of exchange-coupled core/shell MNPs with tailored magnetic properties [28]. The coercive field in these systems can be finely modified through the interface magnetic coupling [29–34], the core size and shell thickness [35–37], or the magnetic anisotropy of the components [23,38–40]. Devices of this type should provide a way to manipulate at will

---

*winkler@cab.cnea.gov.ar

the characteristic switching field of TMR by controlling the magnetic coupling across the core/shell interface. In this way, core/shell nanoparticles combine the properties of multilayer-based tunnel junctions and granular or disordered thin films, offering very high versatility with a simple fabrication process.

Here we report the precise control of the TMR in self-assemblies of half-metallic ferrimagnetic Fe_3O_4 nanoparticles encapsulated in ferrimagnetic electrical insulator $Co_{1-x}Zn_xFe_2O_4$ ($0 \leq x \leq 1$). Progressive replacement of Co^{2+} by Zn^{2+} in the shell reduces the magnetic anisotropy and shifts the maximum of the TMR of the self-assembled device in a perfect correlation with the magnetic response. These results demonstrate the feasibility of tuning the TMR switching field in self-assembled devices formed by magnetic core/shell nanoparticles.

II. EXPERIMENTAL PROCEDURE

$Fe_3O_4/Co_{1-x}Zn_xFe_2O_4$ core/shell nanoparticles are fabricated by seed-mediated high-temperature decomposition of metal-acetylacetonates in benzyl ether assisted by oleic acid and oleylamine, based on the method described in Refs. [39,41,42]. Initially, monodisperse Fe_3O_4 seeds are obtained by mixing 12 mmol of Fe(III) acetylacetonate [Fe(acac)$_3$] with 24 mmol of 1,2-octanediol, 210 mmol benzyl ether, 8 mmol oleic acid, and 40 mmol oleylamine into a three-neck flask, under N_2 flow. The mixture is slowly heated up to the reflux temperature (295 °C) and held for a total time of 120 min. Then the solution containing the nanoparticles is separated into five portions in order to overgrow the spinel ferrite shell. At this point, 0.6 mmol of Co(II) acetylacetonate [Co(acac)$_2$] and Zn(II) acetylacetonate [Zn(acac)$_2$] are added to the mixture, according to a nominal molar ratio $Co_{1-x}Zn_xFe_2O_4$, together with Fe(acac)$_3$ (1.2 mmol), 1,2-octanediol (3 mmol), oleic acid (3 mmol), oleylamine (3 mmol) and benzyl ether (210 mmol), and the heating procedure is repeated. Five samples with Zn nominal concentration $x = 0.00, 0.25, 0.50, 0.75,$ and 1.00 are synthesized. The samples are washed by adding ethanol and centrifuged, followed by the addition of acetone, and magnetically separated. Finally, the MNPs are dispersed in hexane. The nanoparticle compositions are determined with an inductively coupled optical emission spectrometer, brand Agilent model 5110. To perform the measurements, the samples are processed with a Berghoff microwave digester model SW4 in an acid mixture with HNO$_3$: HCl 4 : 1.

The self-assembly of the core/shell MNPS is done at the liquid-air interface following the procedure reported in Refs. [20–22]. In the assembly process schematized in the upper panel of Fig. 1, a drop of 10 μl of solution with 5 mg/ml of nanoparticles in hexane is drop casted onto the surface of triethylene glycol in a Teflon container, which is then covered by a glass slide. In order to transfer the assemblies to a substrate, the Teflon vessel of $1.5 \times 1.5 \times 1.0$ cm^3 is designed with a 30° inclined base plane where the substrate is located previously and is completely covered by the triethylene glycol. A self-assembled structure is formed after complete evaporation of hexane (between 10–15 min). After that the triethylene glycol is removed very slowly using a syringe in order to gently deposit the assembled film on the substrate. All the samples received a thermal treatment in a vacuum atmosphere (approximately 10^{-3} Torr) in order to reduce the organic coating of the particles and to promote a closer contact between them. The decomposition temperature of the organic nanoparticle coating is determined from thermogravimetric analysis. The self-organized nanoparticles are heated from room temperature up to 400 °C at heating rate of 15 °C/min, kept at 400 °C by 30 min and then cooled to room temperature at 15 °C/min.

Structural characterization of core/shell powder samples is performed by conducting XRD experiments on a PANAlytical X′Pert diffractometer with Cu Kα radiation using a glass sample holder (step size 0.026°, range 15°–90°). Transmission electron microscopy (TEM) images and electron diffraction patterns of powder samples and self-assembled nanoparticles are taken in a Philips CM200 transmission electron microscope equipped with an Ultra-Twin lens operating at 200 kV and a resolution of 0.19 nm. In order to perform the structural characterization of the self-assemblies of core/shell nanoparticles, they are transferred from the triethylene glycol surface to commercial silicon nitride TEM grids followed by thermal annealing. Atomic force microscopy (AFM) measurements are done in a Veeco Dimension 3100 SPM in tapping mode using a standard tip. The 2-μm scans are done using a scan frequency of 1 Hz and after waiting 30 min for thermal stabilization and noise reduction. No modification of the surface is observed after the measurements.

The magnetic properties are studied using a commercial superconducting quantum interference device magnetometer (SQUID, MPMS Quantum Design). To perform the measurements the self-assembled nanoparticles are transferred from the triethylene glycol surface to glass substrate (4×6 mm^2) followed by the thermal annealing. The magnetoresistive devices are fabricated by thermal evaporation of the Au/Cr electrodes on glass substrates. The Au/Cr patterns of 7-μm channel length and 6-mm channel width, are fabricated by photolithography as shown in the middle panel of Fig. 1. Then, the self-assembled core/shell nanoparticles floating on the triethylene glycol surface are transferred to the prepatterned glass substrates, and the obtained films are thermally annealed. The magnetotransport measurements are performed using a Keithley 4200 source-measure unit in a two-probe configuration, with a maximum applied field of ± 12 kOe.
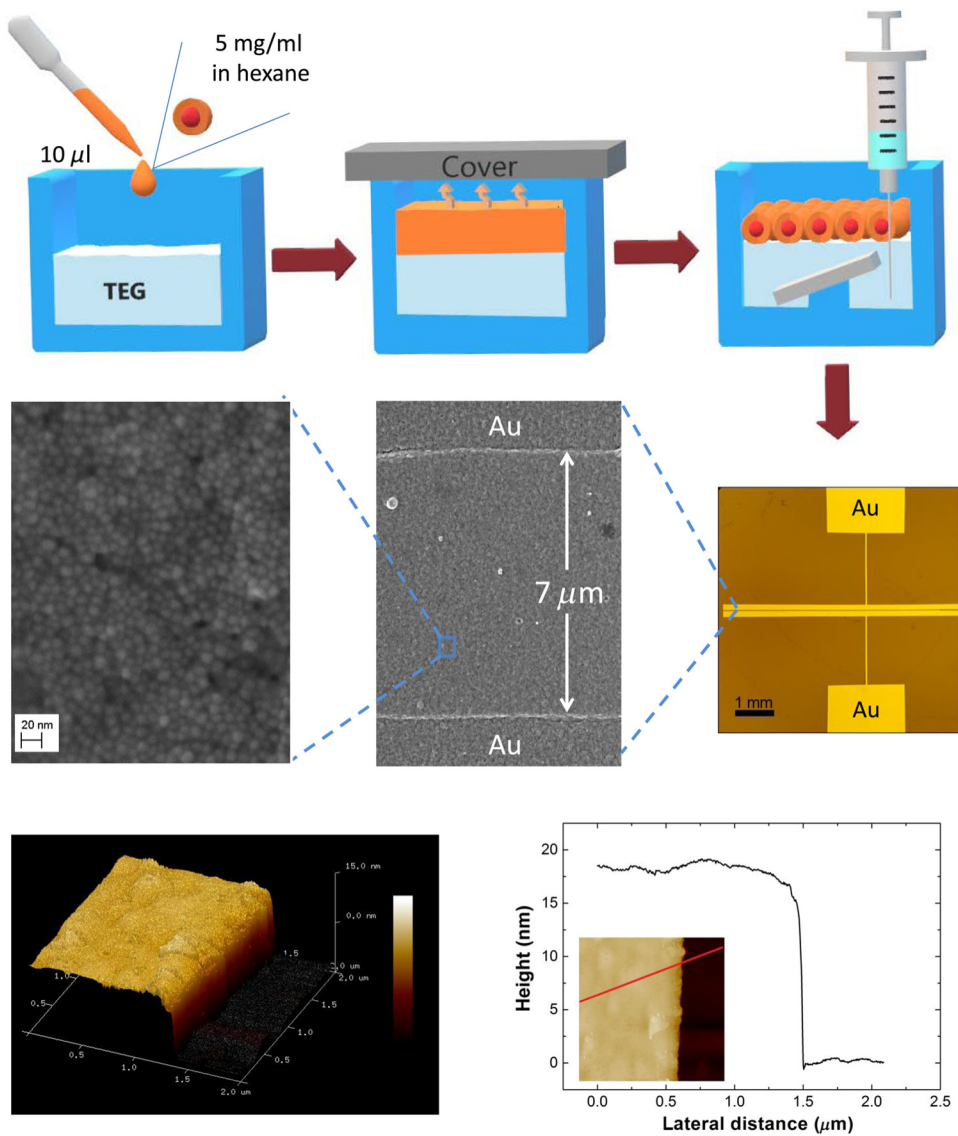
FIG. 1. Scheme of the process of self-assembly of the particles at the liquid-air interface and the transfer of the assemblies on a substrate. The middle part of the figure shows an optical image (right), along with two SEM images of the glass substrate patterned with Au electrodes, separated by 7 μm, with the self-assembled nanoparticles deposited on top. The bottom part of the figure shows the topography and height profile cross section of the annealed nanoparticles assemblies analyzed by AFM. The height profile across the film edge shows a thickness of approximately 20 nm, consistent with a two-layer assembly.

III. RESULTS AND DISCUSSION

Figure 2 compares the morphology and size, measured by TEM, of Fe_3O_4 nanoparticle seeds with a representative core/shell system, $Fe_3O_4/CoFe_2O_4$, both samples are subjected to the same thermal annealing at 400 °C in vacuum atmosphere. From the size histograms, fitted with a Gaussian function, the mean particle sizes ($\langle D \rangle$) are calculated, resulting 7.7 and 9.6 nm, for core and core/shell systems, respectively. From the HRTEM image it is noticed that the core is monocrystalline and the shell growth is epitaxial over the core for most of the nanoparticles. Moreover, different crystalline orientations for the core and shell can be observed for most of the nanoparticles as noticed in Fig. 2(d) where the (044) and (222) crystalline planes of spinel phase are signaled for the core and shell, respectively. The core/shell structure is confirmed by dark field, as shown in Fig. 2(e) where the TEM image is recorded with a small objective aperture positioned on the (113) brighter

electron diffraction ring of the spinel phase. In this way the bright contrast in the reconstructed image corresponds to the spinel grains with the selected crystallographic orientation as schematically drawn in Figs. S1(d–e) (see the Supplemental Material [43]). From the HRTEM and dark-field TEM images, and from the comparison with the core size, the thickness of the $Co_{1-x}Zn_xFe_2O_4$ shell is estimated as approximately 1 nm. The composition of the nanoparticles is analyzed by inductively coupled plasma optical emission spectrometry. From this analytical technique, the concentration of the transition metal ions for all the samples are obtained and reported in Table I. From these data, and assuming a Fe_3O_4 core of 7.7 nm diameter, we calculate the shell stoichiometry, which shows a systematic evolution consistent with the nominal concentration.

The self-assemblies of Fe_3O_4-core/$Co_{1-x}Zn_xFe_2O_4$-shell nanoparticles are obtained by the liquid-air interface process [20–22] as explained in Sec. 2. In order to
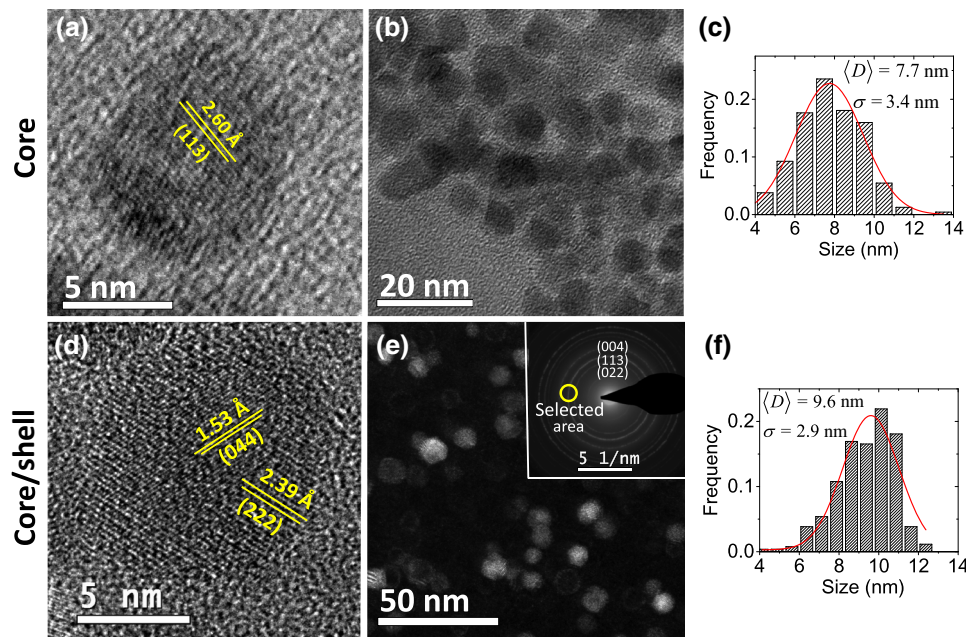
FIG. 2. Top panels: (a),(b) TEM images of the Fe_3O_4 core nanoparticles annealed at $400°$ in vacuum atmosphere, HRTEM where the interplanar distance of (113) spinel phase are signaled, and (c) size histogram fitted with a Gaussian function. Bottom panels: (d) HRTEM image of $Fe_3O_4/CoFe_2O_4$ nanoparticles annealed at $400°$ in vacuum atmosphere, where different crystalline orientations (044) and (222) of spinel structure for the core and shell are indicated. (e) Dark-field TEM image reconstructed with a fraction of the (113) of the spinel diffraction ring and (f) size dispersion for the core/shell nanoparticles with the corresponding Gaussian fitting.

perform the different measurements, the self-assembly and the subsequent thermal treatment is reproduced using a commercial silicon nitride support grid for TEM characterization, and a glass substrate patterned with two Au electrodes separated by approximately 7 μm (as shown in the SEM image of Fig. 1) for the magnetotransport studies. The topography of the annealed assemblies is analyzed by atomic force microscopy. Images acquired at different regions of the films reveal a large homogeneity with uniform and smooth surface, as observed in the bottom panel of Fig. 1. From the AFM height profile cross section at the film boundary, an average film thickness of 20 nm is measured, which corresponds to two layers of nanoparticles.

Homogeneity and narrow-size distribution are essential conditions to reach a large area of self-organization; for core/shell nanoparticles, as observed from Figs. 3 and S1(a) (see Supplemental Material [43]), assemblies of several microns are obtained. From Fig. S1(f) it is also noticed

that the self-organized nanoparticles are separated by a gap of approximately 1 nm. As the thermogravimetric analysis indicates that approximately 7% of residual mass remains in the systems after the thermal treatment at $400°C$ in vacuum atmosphere, and infrared spectroscopy measurements do not detect organic molecules (see Fig. S3 within the Supplemental Material [43]), we conclude that the gap between the nanoparticles is formed by amorphous carbon. The nanoparticle size distributions measured from the TEM micrographs, are shown in the middle panels of Fig. 3. From the fitting of the histograms with a Gaussian function, the mean nanoparticle size $\langle D \rangle$ is calculated and summarized in Table II, which varies between 9.2–9.9 nm for all the systems. We also notice that the nanoparticle size and also the superstructure of the self-assembly is preserved at higher annealing temperature, however at $600°C$ the nanoparticles start to coalesce (see Fig. S2 within the Supplemental Material [43]). From the HRTEM images (shown in Fig. 2 for $x = 0$ and in Fig. 3 for $x = 0.75$ and $x = 1$) it is observed that the core/shell microstructure is preserved after the annealing at $400°C$, where different interplanar distances and crystallographic plane orientation for the inner and outer part of the particle can be measured. As mentioned before, this morphology is confirmed by dark-field images, as shown in Fig. 3 for $x = 0.00$, 0.25, and 0.50. Although the core/shell microstructure is preserved, we can not discard some degree of interdiffusion at the interface as reported for similar nanoparticles systems [44,45]; however, as we discuss later, the magnetoresistance measurements confirm the half-metallic nature of the Fe_3O_4 core.

Figures 4(a) and S4 (see the Supplemental Material [43]) show the magnetization hysteresis loops of the annealed self-assembled nanoparticles, measured with the
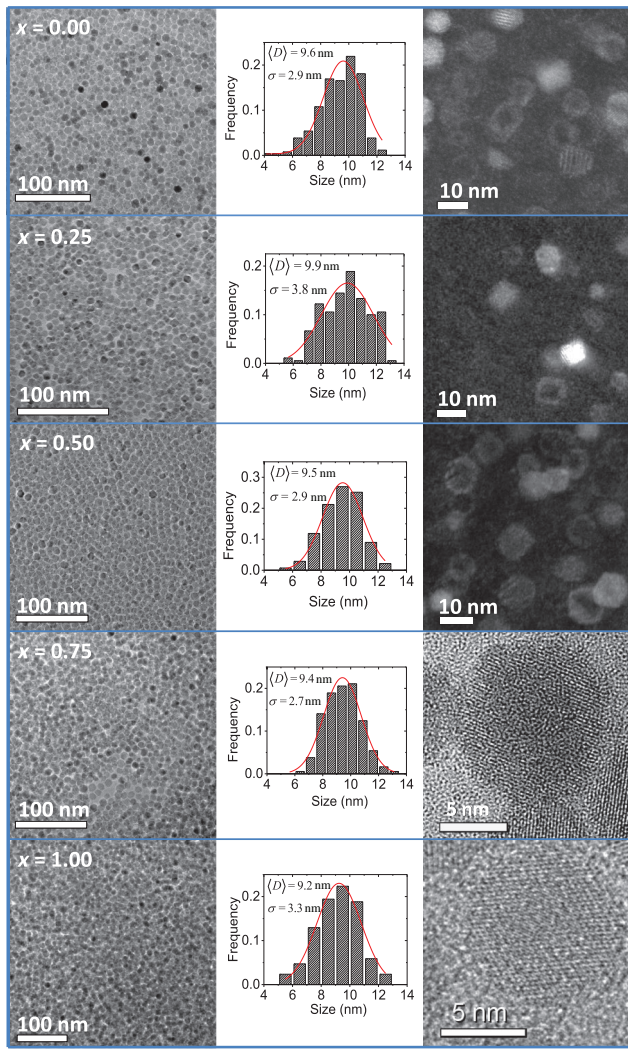
TABLE I. Total concentration of transition metal ions in core-shell nanoparticles measured from inductively coupled plasma mass spectrometry. The last column presents the calculated shell stoichiometry considering the mean nanoparticle size obtained by TEM and a Fe_3O_4 core of 7.7 nm diameter.

Samples	Total concentration			Calculated
	%Co	%Zn	%Fe	Shell stoichiometry
$x = 0.00$	9.40	0.00	90.60	$Co_{0.61}Fe_{2.39}O_4$
$x = 0.25$	7.71	2.36	89.93	$Co_{0.45}Zn_{0.15}Fe_{2.40}O_4$
$x = 0.50$	6.01	4.80	89.19	$Co_{0.39}Zn_{0.35}Fe_{2.26}O_4$
$x = 0.75$	2.68	5.78	91.54	$Co_{0.18}Zn_{0.44}Fe_{2.38}O_4$
$x = 1.00$	0.00	9.94	90.06	$Zn_{0.80}Fe_{2.20}O_4$

FIG. 3. TEM images of the self-assembled $Fe_3O_4/Co_{1-x}Zn_xFe_2O_4$ core/shell nanoparticles for the different compositions from $x = 0$ to $x = 1$, along with the corresponding size distribution histograms. The right panel shows representative images where the core/shell structure can be appreciated from dark-field images for $x = 0$, 0.25 and 0.50 and from high-resolution TEM for $x = 0.75$ and 1. The bright contrast in the dark-field images corresponds to the spinel grains with the particular crystallographic orientation selected by positioning the small objective TEM aperture on the brighter (113) electron diffraction ring of the spinel phase.

TABLE II. Nanoparticle size distribution parameters of Fe_3O_4 and $Fe_3O_4/Co_{1-x}Zn_xFe_2O_4$ obtained from the TEM images, where $\langle D \rangle$ is the mean particle size, and σ is the standard deviation. The last columns present the mean blocking temperature $\langle T_B \rangle$ and the effective magnetic anisotropy constant K_{eff} calculated from the zero-field-cooled (ZFC) and field-cooled (FC) magnetization curves.

Sample	$\langle D \rangle$ (nm)	σ (nm)	$\langle T_B \rangle$ (K)	K_{eff} (10^6 erg/cm^3)
Fe_3O_4	6.9	2.6	17	0.32
$x = 0.00$	9.6	2.9	191	1.54
$x = 0.25$	9.9	3.8	171	1.25
$x = 0.50$	9.5	2.9	135	1.12
$x = 0.75$	9.4	2.7	115	0.99
$x = 1.00$	9.2	3.3	8	0.07

insulator $CoFe_2O_4$ [20]. In contrast, in the core/shell morphology, both phases are strongly coupled at the interface and homogeneous loop is obtained even in the as-synthesized system as shown in Fig. S5 (see the Supplemental Material [43]). The magnetization inversion process of $Fe_3O_4/Co_{1-x}Zn_xFe_2O_4$ core/shell nanoparticles can be analyzed from the theoretical approach developed for bimagnetic soft/hard exchange-coupled nanostructures [46–50]. From these studies, a critical size for the soft magnetic component, δ_{crit}, is found below which both phases are rigidly coupled by interface exchange interaction and reverse their magnetization in a coherent mode at the nucleation field, H_N. This critical size is approximately twice the magnetic Bloch wall width of the hard phase $\delta_w = \pi\sqrt{A/K}$, where A is the exchange stiffness. In this regime, a single square hysteresis loop is obtained, with $H_C = H_N = 2(K_c f_c + K_{sh} f_{sh})/(M_c f_c + M_{sh} f_{sh})$, where M, f, and K are the magnetization, film thickness (or volume fraction), and magnetic anisotropy of the core (c) and shell (sh), respectively [28,51,52]. Instead, if the size of the soft magnetic phase is larger than δ_{crit}, exchange-spring behavior is found, the magnetization reversal is nonuniform and lower coercivities are obtained [48,49,51]. For $CoFe_2O_4$, the values reported for δ_w span in the range of 13–20 nm [28,53], larger than the diameter of the Fe_3O_4 soft core used in this work. Therefore, rigid exchange coupling of the magnetizations of the core and shell phases is expected. This conclusion is supported by the study of $Fe_3O_4/CoFe_2O_4$ soft/hard bilayers, where a critical thickness of 8 nm is found for the crossover from rigid coupling to exchange-spring behavior as a function of the Fe_3O_4 thickness [54]. Therefore, the decrease of H_C with x can be accounted for by the diminution of the magnetic anisotropy of the shell from approximately 4×10^6 erg/cm^3 for $x = 0$, to approximately 2×10^5 erg/cm^3 for $x = 1$ [55] in agreement with the expression for H_C in the rigid exchange-coupled regime.
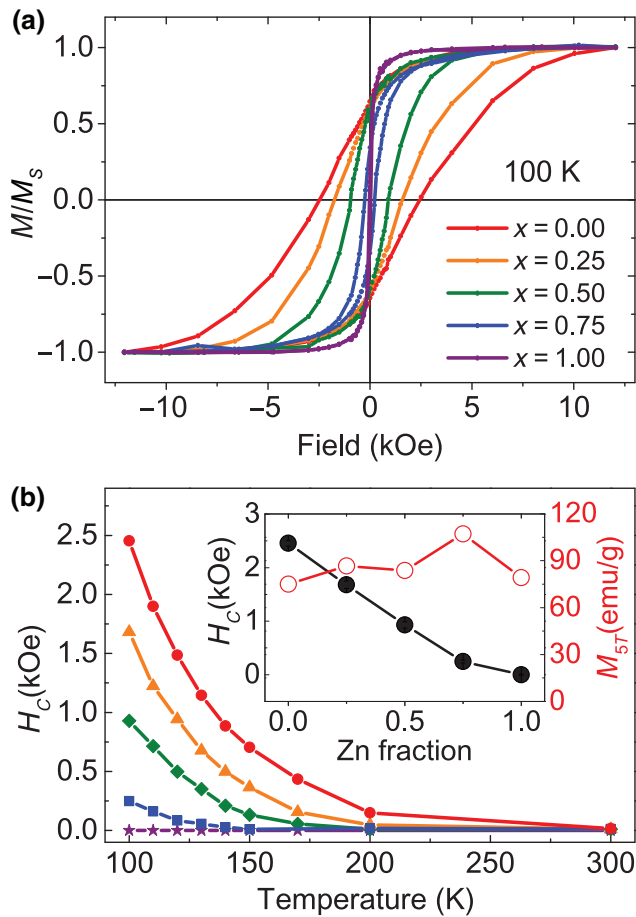
magnetic field applied in the plane of the substrate. The hysteresis loops show a single magnetization reversal for all compositions, with the coercive field (H_C) decreasing approximately linearly with the Zn concentration x, as shown in Fig. 4(b). Notice that the magnetization hysteresis loop reported for binary nanocrystal superlattice $CoFe_2O_4$-Fe_3O_4 results from the superposition of the individual components and an annealing treatment is an essential step to obtain an exchange interaction between the half-metallic Fe_3O_4 and the magnetic

FIG. 4. (a) Hysteresis loops measured at 100 K and (b) coercive field as a function of the temperature for the annealed $Fe_3O_4/Co_{1-x}Zn_xFe_2O_4$ core/shell nanoparticle assemblies. The inset shows the H_C for the annealed self-assembled particles as a function of x, and also the magnetization measured at 5 T (M_{5T}) for the powder sample annealed under the same conditions as the self-assemblies. Both measurements are acquired at 100 K.

increases, which points out that the magnetic behavior is governed by the hard-soft rigid coupling magnetization inversion process, as analyzed previously. However, the annealed assemblies present an approximately 20% larger $\langle T_B \rangle$, H_C and K_{eff}, probably due to an increase of the dipolar interaction and the improvement of the crystallinity in the annealed assemblies.

The magnetic measurements demonstrate that the effective magnetic anisotropy of the system can be controlled by adjusting the shell composition, without appreciably modifying the morphology and the overall magnetic saturation, as observed from the inset of Fig. 4(b). Given that the anisotropy of the system is to a great extent responsible of the switching field of the TMR, devices made of self-assembled core/shell nanoparticles provide an ideal system for studying spin-dependent transport between magnetic nanoparticles. Although both materials at the core-shell structure are strongly exchange coupled and behave as a unique magnetic entity with an average magnetic
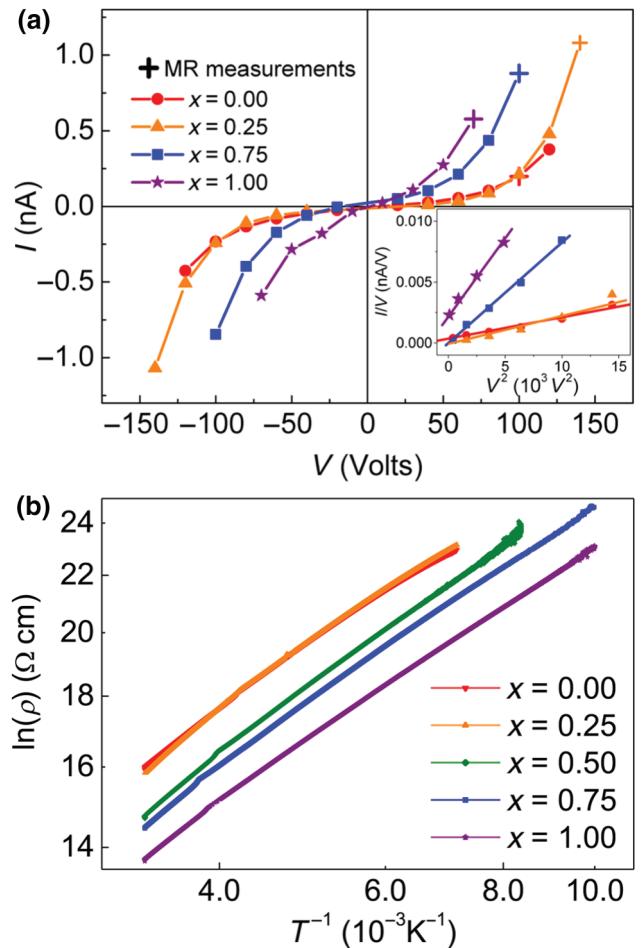
The systematic dependence of the magnetic anisotropy with the shell composition is also reflected in the ZFC and FC magnetization curves shown in Fig. S6 within the Supplemental Material [43]. The temperature where the change from blocked to the superparamagnetic regime is observed decreases progressively with increasing x. From the maximum of the energy barrier distribution calculated as $f(T_B) = (1/T)[d(M_{ZFC} - M_{FC})/dT]$ the mean blocking temperature, $\langle T_B \rangle$, and the effective magnetic anisotropy constant, $K_{eff} = 27k_B T_B/v$, can be obtained for particles of total volume v, as reported in Table II [56]. For comparison, Table S1 (see the Supplemental Material [43]) reports the parameters that characterize the magnetic properties of dispersed nanoparticles before the annealing process. Both systems, the dispersed nanoparticles and the annealed assemblies, present qualitatively and quantitatively similar behavior, with an enhancement of the effective magnetic anisotropy when the concentration of Co in the shell

FIG. 5. (a) Current-voltage characteristics measured at 100 K for all the $Fe_3O_4/Co_{1-x}Zn_xFe_2O_4$ annealed devices. The inset shows I/V versus V^2. (b) Logarithm of the electrical resistivity as a function of $1/T$, both in logarithmic scale.

anisotropy, the conductivity of each phase is different. While the Fe_3O_4 core is half metallic, the $Co_{1-x}Zn_xFe_2O_4$ shell is a semiconductor. Therefore, in order to observe TMR properties it is crucial to have Fe_3O_4 phase to provide the spin-polarized transport, whereas the role of the shell is to modulate the switching field by tuning the magnetic anisotropy, while acting as a tunnel barrier.

The electronic transport in the annealed self-assembled devices is studied from the current-voltage (I-V) measurements and from the temperature dependence of the resistivity ρ, as reported in Fig. 5. From this figure, it can be affirmed that the electron conduction in the devices is given by two independent mechanisms: thermally activated hopping, which is revealed from the temperature dependence of ρ; and the tunneling conduction manifested by the non-Ohmic behavior in the I-V curve with the characteristic V^3 dependence at low temperature, as discussed next. From the Simmons model, which considers inelastic tunneling across an insulating barrier, the I-V curves can be quantitatively linked to the physical parameters of the system, i.e., the tunnel barrier height (h) and width (w), the effective contact area, etc. [57]. This model also considers the linear dependence approximation of the barrier potential profile with V and w. For a voltage smaller than the

potential barrier, the Simmons model can be approximated with the well-known polynomial relationship [58]:

$$\frac{I}{V} \approx G_0 \left(1 + FV^2\right), \tag{1}$$

where G_0 is the equilibrium conductance and $F \propto \xi^2$, where $\xi = w/h$ is the shape factor of the barrier [59]. From the plot shown in the inset of Fig. 5(a), the shape factor of the barrier is clearly increasing with x. Given that the barrier width is approximately constant for all samples, this reflects a progressive decrease of the tunneling barrier height as the Zn content increases. Considering the geometry of the assemblies devices, i.e., the area measured by SEM and the film thickness obtained by AFM microscopy, we plot $\rho(T)$ in Fig. 5(b), which suggests that a thermally activated transport mechanism is also involved in the conduction of the devices. The temperature dependence follows the relation $\ln(\rho) \propto T^{-1/\alpha}$, where $\alpha = 0.4(1)$ is found as the best fitted parameter for all the systems. This value is close to the dependence found in the Efros variable-range hopping model $\ln(\rho) \propto T^{-1/2}$, [60] and is consistent with the behavior measured in other nanoparticle arrays
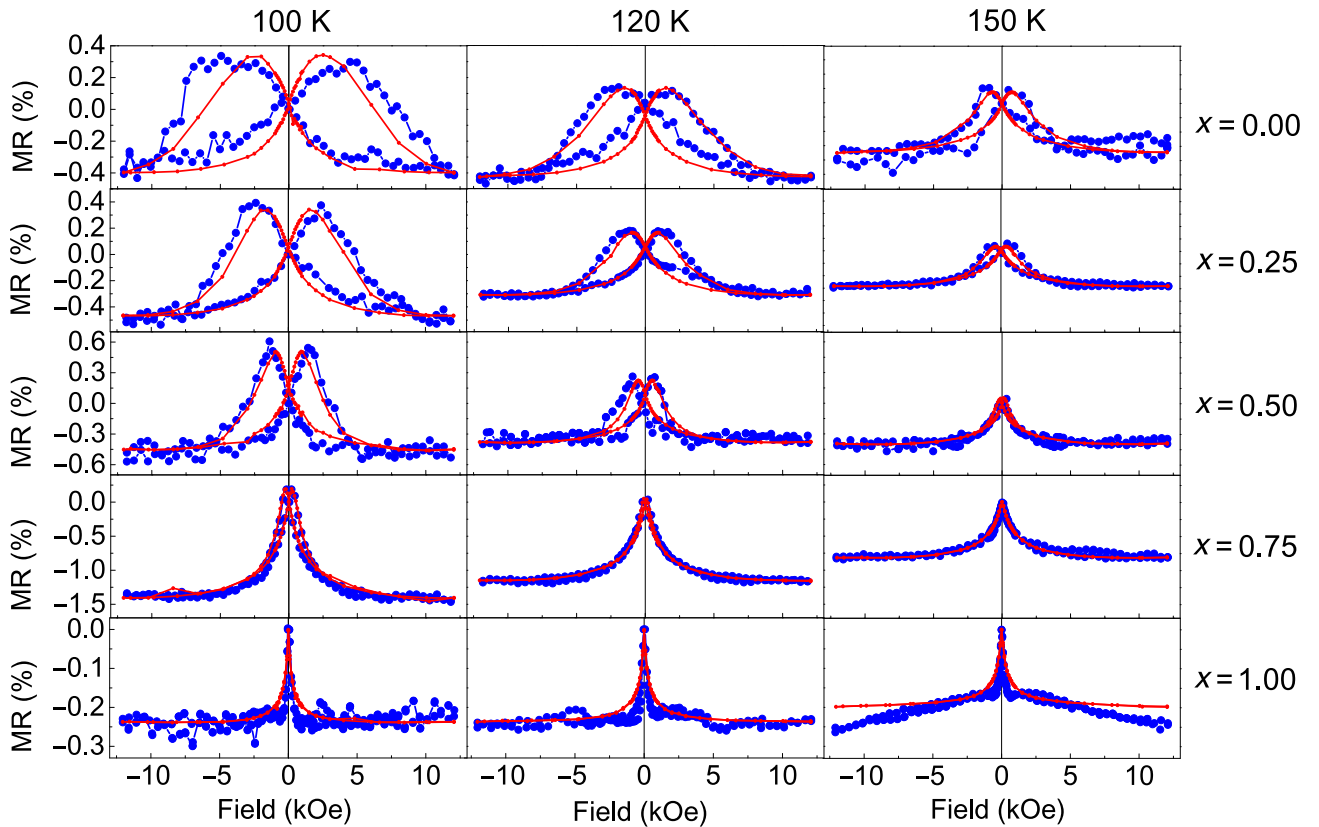

FIG. 6. TMR of the devices studied in this work at different temperatures. The magnetoresistance is defined as $MR = 100 \times [R(H) - R(0)]/R(0)$, and is measured with H in the plane of the self-assembled films. The red line represents the fitting to Eq. 2 using the experimental $M(H)$ curves shown in Fig. 4, measured for each self-assembly of magnetic nanoparticles.

[14,17,21,24,61]. Moreover, $\rho(T)$ in the core/shell assemblies is, at least, 2 orders of magnitude smaller than that reported for pellets of $Co_{1-x}Zn_xFe_2O_4$ powder ferrite [for example, at room temperature $\rho(CoFe_2O_4) \sim 1.10^7$ Ω cm and $\rho(Co_{0.4}Zn_{0.6}Fe_2O_4) \sim 1.10^8$ Ω cm [62–64]]. This result shows that the tunnel conduction strongly increases the conductivity of the core/shell assemblies compared to the values measured in the semiconductor shell material. Notice that the larger the tunneling current, the lower the resistivity of the devices. Therefore, the material that has the lower tunneling barrier will be the one that is most influenced by this contribution. Consistently, from Fig. 5 we measure that the assemblies of nanoparticles with a $ZnFe_2O_4$ shell present the lowest energy barrier, and a systematic increase with decreasing x is observed.

The main findings of this work are summarized in Figs. 6 and 7. Magnetoresistance curves measured at different temperatures for the five devices studied in this work are shown in Fig. 6 and Fig. S7 of the Supplemental

Material [43]. At a given temperature, the switching field of the magnetoresistance curve monotonously decreases when the Zn concentration of the shell increases. Moreover, as shown in Fig. 7, each sample shows a smooth decrease of the switching field with temperature, consistently with the temperature evolution of the coercive field. Also, a saturation behavior of TMR at high magnetic field is observed when x decreases, in good correspondence with the $M(H)$ curves, see Fig. 4.

For spin-polarized intergrain tunneling the TMR is related to the macroscopic magnetization [9,10,25]. For a ferromagnetic insulator granular system, the electron tunneling across the insulating barrier is calculated including an additional exchange energy arising from the interaction between the tunneling electron spin and the nonparallel magnetic moment of the neighboring grains [25,65]. Assuming that the exchange energy can be expressed in terms of the spin correlation function of two ferromagnetic neighboring grains, the magnetoresistance can be expressed as

$$\text{TMR} = -\frac{JP}{4k_BT}[m^2(H,T) - m^2(0,T)], \quad (2)$$

where J accounts for the magnetic correlations when the electron tunnels through the insulating barrier and $m = M/M_S$. Notice that within this model the magnetoresistance does not depend on the total resistivity of the sample. The fittings to this equation using $C = JP/4k_BT$ as the single adjusted parameter for each temperature, are shown in Fig. 6. The good agreement between both measurements from Eq. (2) confirms the spin-polarized tunnel transport in the present devices, where the C parameter gives the proportionality between two independent experiments, $M(H)$ and $\rho(H)$. Moreover, in agreement with Eq. (2), the fittings show that C varies approximately linearly with $1/T$ over the measured temperature range [see Fig. 7(b)]. However, although Eq. (2) adjusts the field and temperature dependence of TMR with the magnetization, due to the complex nature of the present system, it is hard to determine the dependence between the C parameter and the shell stoichiometry. Even though all the systems have the same Fe_3O_4 core, the $Co_{1-x}Zn_xFe_2O_4$ shell is synthesized in a second step, which leads to a shell thickness dispersion along the Zn composition, moreover from the synthesis and later thermal treatment the nanostructures could also present dispersion in the nanoparticle coating. These experimental factors could affect the magnetic correlations when the electron tunnels through the insulating magnetic barrier and also the surface Fe_3O_4 spin polarization. Nevertheless, although it is hard to estimate the evolution of the magnetic correlation with the shell stoichiometry, the magnitude of the interaction can be estimated. Assuming the spin polarization of magnetite, ($P \approx 39\%$) [27] a coupling constant of $J \approx 1.0(0.4)$ meV (approximately

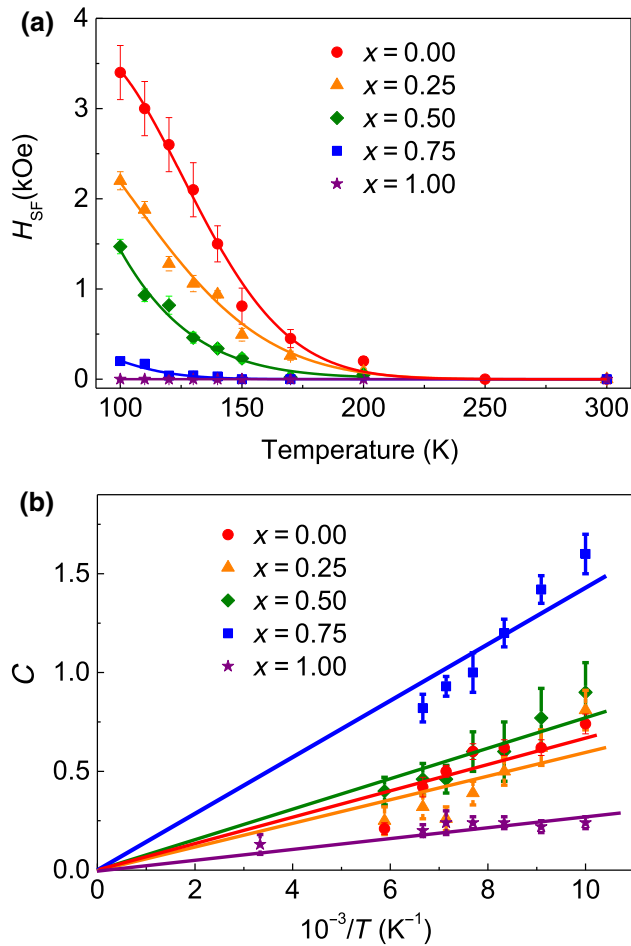FIG. 7. (a) Switching field (H_{SF}) as a function of temperature for $Fe_3O_4/Co_{1-x}Zn_xFe_2O_4$ nanoparticles and (b) $C = JP/4k_BT$ obtained as the adjusted parameter from Eq. (2) as a function of the inverse of the temperature.

10 K) is obtained, comparable to the calculations for the intergrain tunneling transport of manganese perovskites [66].

The TMR amplitude, which is in the 0.3–1.5% range depending on the composition, is similar to other reported values for self-assembled nanoparticles [16,21,24], however, it is much smaller than the calculated from the Julliere model: $TMR = 2P^2/(1 - P^2)$ on the basis of the spin-polarization values of magnetite. This reduction may be due to the fact that the tunneling probability decreases exponentially with the barrier width. According to Refs. [67,68] for TMR multilayers, the optimal barrier thickness is in the 1–1.5 nm range; however, the tunnel current between Fe_3O_4 cores in the self-assembled structure must pass through the insulator barrier of approximately 3 nm width, which is composed by the cobalt ferrite shell and the amorphous carbon nanoparticle coating. On the other hand, although it is known that the TMR diminishes with increasing bias voltage [53], the high resistance of the magnetic nanoparticle devices determines the experimental parameters, and high voltage bias approximately 100 V had to be applied to perform the transport measurements at low temperature. These factors make evident the importance of optimizing the different stages of the fabrication process in order to increase the conductivity to produce large amplitude and low switching-field TMR devices based on core/shell magnetic nanoparticles. However, irrespective of the absolute value of TMR, this study demonstrates that the switching field of TMR can be tailored at will in self-assemblies of exchange-coupled core-shell nanoparticles, synthesized by an affordable chemical route.

IV. CONCLUSION

In summary, we fabricate self-assemblies of core/shell nanoparticles with controlled TMR. Particularly, we show that the magnetic properties can be finely tuned by changing the shell composition, which provides a tool to adjust the TMR switching field. We show that whereas the Fe_3O_4 core provides the spin-polarized transport, the shell acts as a tunnel barrier in the self-assembly and also modulates the switching field by tuning the magnetic anisotropy through the interface exchange coupling. This approach shows the feasibility to use assemblies of exchange-coupled magnetic nanoparticles in TMR devices, where different combinations of soft/hard and hard/soft core/shell configurations can be envisaged. In this way, combinations of materials can be carefully designed to move across the rigid coupling to exchange bias regime, to design devices with tailored magnetotransport response, which gives a promising base for the design of core/shell nanoparticle-based devices for fundamental studies or for spintronic applications.

[1] M. N. Baibich, J. M. Broto, A. Fert, F. Nguyen Van Dau, F. Petroff, P. Etienne, G. Creuzet, A. Friederich, and J. Chazelas, Giant Magnetoresistance of (001)Fe/(001)Cr Magnetic Superlattices, Phys. Rev. Lett. **61,** 2472 (1988).

[2] G. Binasch, P. Grünberg, F. Saurenbach, and W. Zinn, Enhanced magnetoresistance in layered magnetic structures with antiferromagnetic interlayer exchange, Phys. Rev. B **39,** 4828 (1989).

[3] I. Zutic, F. Jaroslav, and S. Das Sarma, Spintronics: Fundamentals and applications, Rev. Mod. Phys. **76,** 323 (2004).

[4] S. D. Bader and S. S. P. Parkin, Spintronics, Annu. Rev. Condens. Matter Phys. **1,** 71 (2010).

[5] M. Julliere, Tunneling between ferromagnetic films, Phys. Lett. A **54,** 225 (1975).

[6] J. S. Moodera, L. R. Kinder, T. M. Wong, and R. Meservey, Large Magnetoresistance at Room Temperature in Ferromagnetic Thin Film Tunnel Junctions, Phys. Rev. Lett. **74,** 3273 (1995).

[7] S. Yuasa, T. Nagahama, A. Fukushima, Y. Suzuki, and K. Ando, Giant room-temperature magnetoresistance in single-crystal Fe/MgO/Fe magnetic tunnel junctions, Nat. Mater. **3,** 868 (2004).

[8] D. D. Djayaprawira, K. Tsunekawa, M. Nagai, H. Maehara, S. Yamagata, N. Watanabe, S. Yuasa, Y. Suzuki, and K. Ando, 230% room-temperature magnetoresistance in CoFeB/MgO/CoFeB magnetic tunnel junctions, Appl. Phys. Lett. **86,** 092502 (2005).

[9] M. A. López-Quintela, L. E. Hueso, J. Rivas, and F. Rivadulla, Intergranular magnetoresistance in nanomanganites, Nanotechnology **14,** 212 (2003).

[10] H. Y. Hwang, S-W. Cheong, N. P. Ong, and B. Batlogg, Spin-Polarized Intergrain Tunneling in $La_{2/3}Sr_{1/3}MnO_3$, Phys. Rev. Lett. **77,** 2041 (1996).

[11] C. B. Murray, C. R. Kagan, and M. G. Bawendi, Synthesis and characterization of monodisperse nanocrystals and close-packed nanocrystal assemblies, Annu. Rev. Mater. Sci. **30,** 545 (2000).

[12] S. Sun, C. B. Murray, D. Weller, L. Folks, and A. Moser, Monodisperse FePt Nanoparticles and Ferromagnetic FePt Nanocrystal Superlattices, Science **287,** 1989 (2000).

[13] H. Zeng, C. T. Black, R. L. Sandstrom, P. M. Rice, C. B. Murray, and Shouheng Sun, Magnetotransport of magnetite nanoparticle arrays, Phys. Rev. B **73**, 020402 (2006).

[14] C. T. Black, C. B. Murray, R. L. Sandstrom, and S. Sun, Spin-dependent tunneling in self-assembled cobalt-nanocrystal superlattices, Science **290**, 1131 (2000).

[15] S. Wang, F. J. Yue, D. Wua, F. M. Zhang, W. Zhong, and Y. W. Du, Enhanced magnetoresistance in self-assembled monolayer of oleic acid molecules on Fe_3O_4 nanoparticles, Appl. Phys. Lett. **94**, 012507 (2009).

[16] J. Dugay, R. P. Tan, A. Meffre, T. Blon, L. M. Lacroix, J. Carrey, P. F. Fazzini, S. Lachaize, B. Chaudret, and M. Respaud, Room-temperature tunnel magnetoresistance in self-assembled chemically synthesized metallic iron nanoparticles, Nano Lett. **11**, 5128 (2011).

[17] K. Mohan Kant, K. Sethupathi, and M. S. Ramachandra Rao, Role of oxide barrier in intergranular tunnel junctions: An enhanced magnetoresistance in SiO_2 and ZnO coated Fe_3O_4 nanoparticle compacts, J. Appl. Phys. **103**, 07F318 (2008).

[18] N. Taub, A. Tsukernik, and G. Markovich, Interparticle spin-polarized tunneling in arrays of magnetite nanocrystals, J. Magn. Magn. Mater. **321**, 1933 (2009).

[19] T. B. Tran, I. S. Beloborodov, Jingshi Hu, X. M. Lin, T. F. Rosenbaum, and H. M. Jaeger, Sequential tunneling and inelastic cotunneling in nanoparticle arrays, Phys. Rev. B **78**, 075437 (2008).

[20] J. Chen, X. Ye, J. O. Soong, J. M. Kikkawa, C. R. Kagan, and C. B. Murray, Bistable Magnetoresistance Switching Binary Nanocrystal Superlattices by Self-Assembly and Thermal Annealing, ACS Nano **7**, 1478 (2013).

[21] A. Dong, J. Chen, J. M. Vora, P. M. Kikkawa, and C. B. Murray, Binary nanocrystal superlattice membranes self-assembled at the liquid-air interface, Nature **466**, 474 (2010).

[22] C. Jiang, C. W. Leung, and P. W. T. Pong, Self-assembled thin films of Fe_3O_4-Ag composite nanoparticles for spintronic applications, Appl. Surf. Sci. **419**, 692 (2017).

[23] P. A. Kumar, S. Ray, S. Chakraverty, and D. D. Sarma, Engineered spin-valve type magnetoresistance in $Fe_3O_4 - CoFe_2O_4$ core-shell nanoparticles, View Appl. Phys. Lett. **103**, 102406 (2013).

[24] Y. Zhang, H. Xing, N. Poudyal, V. Nandwana, C. B. Rong, S. S. Yan, H. Zeng, and J. P. Liu, Inversed tunneling magnetoresistance in hybrid $FePt/Fe_3O_4$ core/shell nanoparticles systems, J. Appl. Phys. **108**, 103905 (2010).

[25] J. S. Helman and B. Abeles, Tunneling of Spin-Polarized Electrons and Magnetoresistance in Granular Ni Films, Phys. Rev. Lett. **37**, 1429 (1976).

[26] M. El-Hilo, R. W. Chantrell, and K. O'Grady, A model of interaction effects in granular magnetic solids, J. Appl. Phys. **84**, 5114 (1998).

[27] G. Hu and Y. Suzuki, Negative Spin Polarization of Fe_3O_4 in Magnetite/Manganite-based Junctions, Phys. Rev. Lett. **89**, 276601 (2002).

[28] Alberto López Ortega, Marta Estrader, German Salazar Alvarez, Alejando G. Roca, and Josep Nogués, Applications of exchange coupled Bi-magnetic hard/soft and soft/hard magnetic core/shell nanoparticles, Phys. Rep. **553**, 1 (2015).

[29] G. C. Lavorato, E. Lima, H. E. Troiani, R. D. Zysler, and E. L. Winkler, Tuning the coercivity and exchange bias by controlling the interface coupling in bimagnetic core/shell nanoparticles, Nanoscale **9**, 10240 (2017).

[30] G. Salazar-Alvarez, J. Sort, S. Suriñach, M. D. Baró, and J. Nogués, Synthesisand size-dependent exchange bias in inverted core/shell MnO/Mn_3O_4 nanoparticles, J. Am. Chem. Soc. **129**, 9102 (2007).

[31] V. Skumryev, S. Stoyanov, Y. Zhang, G. Hadjipanayis, D. Givord, and J. Nogués, Beating the superparamagnetic limit with exchange bias, Nature **423**, 850 (2003).

[32] A. Sarkar, N. Behera, R. Adhikari, and A. K. Das, Studies on nonlinear electrical transport and magnetoresistance in co/coo core-shell nanostructure, AIP Conf. Proc. **1447**, 937 (2012).

[33] E. L. Winkler, E. Lima, Jr., D. Tobia, M. E. Saleta, H. E. Troiani, E. Agostinelli, D. Fiorani, and R. Zysler, Origin of magnetic anisotropy in $ZnO/CoFe_2O_4$ and $CoO/CoFe_2O_4$ core/shell nanoparticle systems, Appl. Phys. Lett. **101**, 252405 (2012).

[34] G. Lavorato, E. Winkler, A. Ghirri, D. Lima, Jr., E. Peddis, H. E. Troiani, D. Fiorani, E. Agostinelli, D. Rinaldi, and R. D. Zysler, Exchange bias and surface effects in bimagnetic CoO-Core/$Co_{0}.5Ni_{0}.5Fe_2O_4$-Shell nanoparticles, Phys. Rev. B **94**, 054432 (2016).

[35] X. Liu, B. P. Pichon, C. Ulhaq, C. Lefèvre, J. M. Grenèche, D. Bégin, and S. Bégin-Colin, Systematic study of exchange coupling in core-shell $Fe_3-\delta O_4/CoO$ nanoparticles, Chem. Mater. **27**, 4073 (2015).

[36] E. Lottini, A. López-Ortega, G. Bertoni, S. Turner, M. Meledina, G. Tendeloo, C. Van de Julián Fernández, and C. Sangregorio, Strongly exchange coupledcore/shell nanoparticles with high magnetic anisotropy: A strategy toward rare-earth-free permanent magnets, Chem. Mater. **28**, 4214 (2016).

[37] Gabriel C. Lavorato, Enio Lima, Jr., Dina Tobia, Dino Fiorani, Horacio E. Troiani, Roberto D. Zysler, and Elin L. Winkler, Size effects in bimagnetic $CoO/CoFe_2O_4$ core/shell nanoparticles, Nanotechnology **25**, 355704 (2014).

[38] M. Sytnyk, R. Kirchschlager, M. I. Bodnarchuk, D. Primetzhofer, D. Kriegner, H. Enser, J. Stangl, P. Bauer, M. Voith, A. W. Hassel, F. Krumeich, F. Ludwig, A. Meingast, G. Kothleitner, M. Kovalenko, and W. Heiss, Tuning the magnetic properties of metal oxide nanocrystal heterostructures by cation exchange, Nano. Lett. **13**, 586 (2013).

[39] F. Fabris, E. Lima, Jr., E. De Biasi, H. E. Troiani, M. Vasquez Mansilla, T. E. Torres, R. Fernández-Pacheco, M. R. Ibarra, G. F. Goya, R. Zysler, and E. Winkler, Controlling the dominant magnetic relaxation mechanisms for magnetic hyperthermia in bimagnetic core-shell nanoparticles, Nanoscale **11**, 3164 (2019).

[40] G. C. Lavorato, E. Lima, H. E. Troiani, R. D. Zysler, and E. L. Winkler, Exchange-coupling in thermal annealed bimagnetic core/shell nanoparticles, J. Alloys. Compd. **633**, 333 (2015).

[41] S. Sun and H. Zeng, Size-controlled synthesis of magnetite nanoparticles, J. Am. Chem. Soc. **124**, 8204 (2002).

[42] S. H. Sun, H. Zeng, D. B. Robinson, S. Raoux, P. M. Rice, S. X. Wang, and G. X. Li, Monodisperse MFe_2O_4 (M = Fe, Co, Mn) nanoparticles, J. Am. Chem. Soc. **126**, 273 (2004).

[43] See Supplemental Material at http://link.aps.org/supplemental/10.1103/PhysRevApplied.11.054089 for additional microstructural information of the core/shell nanoparticle assemblies annealed at different temperatures, obtained by TEM and HRTEM. Further characterization of the as-synthetized and annealed $Fe_3O_4/CoFe_2O_4$ core-shell nanoparticle by thermogravimetric (TGA) and infrared (FT IR) measurements, and additional magnetic characterization, as the hysteresis cycles as a function of the temperature and ZFC and FC magnetization curves of the annealed nanoparticles, it is also included. See also details of the magnetoresistance temperature evolution of the self-assemblies.

[44] A. López-Ortega, M. Estrader, G. Salazar-Alvarez, S. Estradé, I. V. Golosovsky, R. K. Dumas, D. J. Keavney, M. Vasilakaki, K. N. Trohidou, J. Sort, F. Peiró, S. Suriñach, M. D. Baró, and J. Nogués, Strongly exchange coupled inverse ferrimagnetic soft/hard $Mn_xFe_{3-x}O_4/Fe_xMn_{3-x}O_4$ core/shellheterostructured nanoparticles, Nanoscale **4**, 5138 (2012).

[45] K. L. Krycka, J. A. Borchers, G. Salazar-Alvarez, A. López-Ortega, M. Estrader, S. Estradé, E. Winkler, R. D. Zysler, J. Sort, F. Peiró, M. D. Baró, C. C. Kao, and J. Nogués, Resolving material-specific structures with in $Fe_3O_4/\gamma - Mn_2O_3$ core/shell nanoparticles using anomalous small-anglex-ray scattering, ACS Nano **7**, 921 (2013).

[46] R. Skomski and J. M. D. Coey, Giant energy product in nanostructured two-phase magnets, Phys. Rev. B **48**, 15812 (1993).

[47] E. F. Kneller and R. Hawig, The exchange-spring magnet: A new material principle for permanent magnets, IEEE Trans. Magn. **27**, 3588 (1991).

[48] G. P. Zhao and X. L. Wang, Nucleation, pinning, and coercivity in magnetic nanosystems: An analytical micromagnetic approach, Phys. Rev. B **74**, 012409 (2006).

[49] G. P. Zhao, M. G. Zhao, H. S. Lim, Y. P. Feng, and C. K. Ong, From nucleation to coercivity, Appl. Phys. Lett. **87**, 162513 (2005).

[50] T. Leineweber and H. Kronmüller, Micromagnetic examination of exchange coupled ferromagnetic nanolayers, J. Magn. Magn. Mater. **176**, 145 (1997).

[51] Eric E. Fullerton, J. S. Jiang, and S. D. Bader, Hard/soft magnetic heterostructures: Model exchange-spring magnets, J. Magn. Magn. Mater. **200**, 392 (1999).

[52] G. P. Zhao, X. L. Wang, Y. P. Feng, and C. W. Huang, Coherent rotation and effective anisotropy, IEEE Trans. Magn. **43**, 2908 (2007).

[53] J. M. D. Coey, *Magnetism and Magnetic Materials* (Cambridge University Press, Cambridge, 2010).

[54] G. Lavorato, E. Winkler, B. Rivas-Murias, and F. Rivadulla, Thickness dependence of exchange coupling in epitaxial $Fe_3O_4/CoFe_2O4$ soft/hard magnetic bilayers, Phys. Rev. B **94**, 054405 (2016).

[55] S. Bullita, A. Casu, M. F. Casula, G. Concas, F. Congiu, A. Corrias, A. Falqui, D. Loche, and C. Marras, $ZnFe_2O_4$ nanoparticles dispersed in a highly porous silica aerogel matrix: A magnetic study, Phys. Chem. Chem. Phys. **16,** 4843 (2014).

[56] J. Dormann, F. D'Orazio, F. Lucari, E. Tronc, P. Prené, J. Jolivet, D. Fiorani, R. Cherkaoui, and M. Noguès, Thermal variation of the relaxation time of the magnetic moment of γ-Fe_2O_3 nanoparticles with interparticle interactions of various strengths, Phys. Rev. B **53**, 14291 (1996).

[57] J. G. Simmons, Generalized formula for the electric tunnel effect between similar electrodes separated by a thin insulating film, J. Appl. Phys. **34**, 1793 (1963).

[58] J. G. Simmons, Low-voltage current-voltage relationship of tunnel junctions, J. Appl. Phys. **34**, 238 (1963).

[59] A. Vilan, Analyzing molecular current-voltage characteristics with the Simmons tunneling model: Scaling and linearization, J. Phys. Chem. C **111**, 4431 (2007).

[60] A. L. Efros and B. I. Shklovskii, Coulomb gap and low temperature conductivity of disordered systems, J. Phys. C: Solid State Phys. **8**, L49 (1975).

[61] N. N. Song, H. T. Yang, F. Y. Li, Z. A. Li, W. Han, X. Ren, Y. Luo, X. C. Wang, C. Q. Jin, X. Q. Zhang, and Z. H. Cheng, Interspacing dependence of spin-dependent variable range hopping for cold-pressed Fe_3O_4 nanoparticles, J. Appl. Phys. **113**, 184309 (2013).

[62] R. Rani, G. Kumar, K. M. Batoo, and M. Singh, Electric and dielectric study of zinc substituted cobalt nanoferrites prepared by solution combustion method, Am. J. Nanomater. **1**, 9 (2013).

[63] I. H. Gul, A. Z. Abbasi, F. Amin, M. Anis ur Rehman, and A. Maqsood, Structural, magnetic and electrical properties of $Co_{1-x}Zn_xFe_2O_4$ synthesized by co-precipitation method, J. Magn. Magn. Mater. **311**, 494 (2007).

[64] A. V. Ramana Reddy, G. Ranga Mohan, B. S. Boyanov, and D. Ravinder, Electrical transport properties of zinc-substituted cobalt ferrites, Mater. Lett. **39**, 153 (1999).

[65] S. Barzilai, Y. Goldstein, I. Balberg, and J. S. Helman, Magnetic and transport properties of granular cobalt films, Phys. Rev. B **23**, 1809 (1981).

[66] L. L. Balcells, J. Fontcuberta, B. Martinez, and X. Obradors, Magnetic surface effects and low-temperature magnetoresistance in manganese perovskites, J. Phys.: Condens. Matter **10**, 1883 (1998).

[67] J. S. Moodera, E. F. Gallagher, K. Robinson, and J. Nowak, Optimum tunnel barrier in ferromagnetic-insulator-ferromagnetic tunneling structures, Appl. Phys. Lett. **70**, 3050 (1997).

[68] S. Joo, K. Y. Jung, K. I. Jun, D. S. Kim, K. H. Shin, J. K. Hong, B. C. Lee, and K. Rhie, Spin-filtering affect of thin Al_2O_3 barrier on tunneling magnetoresistance, Appl. Phys. Lett. **104**, 152407 (2014).